ELSEVIER

Three-dimensional rate-dependent crystal plasticity based on Runge–Kutta algorithms for update and consistent linearization

J.L. Raphanel [a,*], G. Ravichandran [b], Y.M. Leroy [a]

[a] *Laboratoire de Mécanique des Solides (LMS), CNRS UMR No. 7649, Ecole Polytechnique, 91128 Palaiseau Cedex, France*
[b] *Graduate Aeronautical Laboratories, California Institute of Technology, Pasadena, CA 91125, USA*

Abstract

A new algorithm for three-dimensional rate dependent crystal plasticity is presented which involves first, the explicit update of the dependent variables based on a high-order accurate scheme and second, the derivation of the consistent operator by the lineariziation of this update algorithm, in order to warrant a quadratic rate of convergence during the iterative equilibrium search. A detailed and complete description of the governing equations amenable to numerical implementation is provided using the convected coordinate formalism. The algorithm has been implemented for an update based on the second-order accurate Runge–Kutta integration scheme in a displacement based finite-element code. The methodology for extending the algorithm to the fourth-order accurate Runge–Kutta scheme is discussed. The algorithm is illustrated for one-dimensional loading of otherwise traction free single crystals loaded along specific crystallographic directions and for a 3D simulation of a tension test for a face centered cubic single crystal oriented for symmetric double slip up to the onset of shear localization. These first numerical simulations are consistent with the analytical solutions. For the 3D case, they provide an insight on the development of plasticity through the sample, with an initial first phase leading to an homogeneous deformation, followed by a second phase where the deformation is more and more limited to the central sections of the sample and ultimately becomes localized, without the need for any initial defect or perturbation.
© 2004 Elsevier Ltd. All rights reserved.

Keywords: Algorithms; Crystals; Finite deformation; Finite element; Plasticity

1. Introduction

Plasticity theory for crystalline materials has been an active area of research in both mechanics and materials, see for example, Asaro (1983), Havner (1992), Bassani (1993) and Kocks et al. (2000). In

---

* Corresponding author. Tel.: +33-1-6933-3391; fax: +33-1-6933-3026.
E-mail address: raphanel@lms.polytechnique.fr (J.L. Raphanel).

particular, the last two decades have witnessed considerable progress that has been made in numerical modeling of crystal plasticity using various approaches. This has been instrumental for making advances in problems related to polycrystals, texture evolution, metal forming, geological structures, and numerous other areas of applications.

The early concepts of crystal plasticity and geometry of slip dates back to the contributions of Taylor, Schmid and their coworkers (e.g., Taylor and Elam, 1923; Schmid and Boas, 1935). Taylor first postulated that five independent slip systems are needed to accommodate an arbitrary strain increment imposed on a crystal (Taylor, 1938). The Schmid law states that in response to applied loads on a single crystal, slip occurs when the resolved shear stress on a crystallographic slip system (uniquely defined by a slip direction and a slip plane normal) exceeds a critical value that is a material property (Schmid and Boas, 1935). Subsequently, much of the work in crystal plasticity was related to metal forming, particularly rolling experiments and their interpretation within the context of active slip systems, Taylor factor, averaging the response of crystals, texture development and other related issues. It was recognized early that crystalline slip could induce finite deformation in the crystal and particularly large rotations associated with slip. However, small strain theory was applied to modeling the response of such crystals including rotations and as a result, simple solutions could be constructed (e.g., Reid, 1973) which helped to gain insights into material behavior and processes. In the early 70s, considerable progress was made in developing a continuum framework for modeling finite deformation and associated constitutive laws for crystalline solids, which were due to Rice (1971) and Hill and Rice (1972); also, see Mandel (1965) and Hill (1966) for small deformation and Teodosiu and Sidoroff (1976) and Asaro and Rice (1977) for finite strain formulation.

The continuum mechanics framework provided the necessary foundations to develop a systematic computational methodology for performing the first detailed numerical simulations of single crystals including their localization behavior (Peirce et al., 1982). Early simulations were 2D plane strain based on the Asaro's (1979) planar double slip model and provided insights concerning nonuniform and localized deformation in single crystals. They were further extended to include modeling of polycrystals and other problems of interest. Due to increase in computational resources that became available, full scale three-dimensional simulations of crystalline solids undergoing multislip (fcc, bcc) became increasingly feasible (e.g., Cuitiño and Ortiz, 1992; Kalidindi et al., 1992). However, the complexity of the structure of governing equations and large number of internal variables in crystal plasticity models generally make the 3D numerical simulations intensive and time consuming.

Two distinct approaches have been followed in developing numerical methods for rate dependent crystal plasticity problems, based either on explicit or implicit schemes for both the time integration of the incremental constitutive relations (called the update) and the equilibrium search. The computations of Asaro, Needleman and coworkers (e.g., Peirce et al., 1982; Needleman et al., 1985) on crystal plasticity follow essentially the explicit forward gradient method proposed by Peirce et al. (1984). This rate tangent modulus method was effectively used in simulating challenging problems such as strain localization of crystals in 2D. Such explicit methods involve no iterations and hence are extremely efficient, but, are inherently first-order accurate and may require very small time steps for the solution to remain close to the equilibrium. Implicit schemes have also been developed for rate dependent crystal plasticity problems (e.g., Cuitiño and Ortiz, 1992; Kalidindi et al., 1992). These schemes involve iterations both at the local level to update the stress and globally to enforce equilibrium, requiring thus more computational effort than the explicit schemes. They remain first-order accurate and hence may require sufficiently small increments in loading to ensure convergence, both locally and globally. As three-dimensional modeling of processes and structures become more and more widespread, as it is the case in multiscale or hierarchical modeling, numerical algorithms with increased efficiency, speed and enhanced accuracy become more desirable. Here, a new algorithm based on the Runge–Kutta method for update and consistent linearization for three-dimensional rate-dependent crystal plasticity problems is presented. Runge–Kutta scheme is a standard and well known integration method for differential equations and the characteristics of the scheme including

error estimates are well established. The Runge–Kutta method provides an explicit update method and is based on known or projected values for quantities of interest at various times within a time step. The novelty, and the difficulty of the proposed scheme, resides with the analytical expression of the consistent tangent moduli (Simo and Taylor, 1985) which are derived by linearizing the constitutive update obtained with the Runge–Kutta integration scheme. Thus, in addition to a robust and classical explicit update, a quadratic rate of convergence is attained during the equilibrium search.

The fundamentals of crystal plasticity and governing equations are briefly discussed in Section 2. In Section 3, the computational algorithm for update and construction of the consistent tangent is presented and discussed in the context of the second-order Runge–Kutta method. Details of the computational scheme are also discussed in this section. Specific choices for hardening and viscosity laws that are used in the simulations are outlined in Section 4. This is followed in Section 5 by illustrative examples of simulations on fcc single crystals subjected to uniaxial tension, compression and shear. In addition, results from a full scale 3D simulation of a fcc single crystal up to the onset of strain localization are discussed. The conclusions are presented in Section 6. The convected coordinates formalism that is employed in the formulation of the tangent operators, detailed expressions for the components of the consistent tangent, extension of the proposed algorithm to a fourth-order accurate scheme and analytical solutions for rigid plastic rate independent fcc crystal subjected to uniaxial loading, are presented in the Appendices A, B, C, D, respectively, for sake of completeness.

2. Kinematics and constitutive framework for crystal plasticity

The objective of this section is to present concisely the continuum theory of crystal plasticity which has been implemented in the proposed numerical algorithm. A finite-deformation constitutive framework was proposed by Rice (1971) and Hill and Rice (1972) and a summary of the line of research which leads to our current understanding of crystal plasticity is found in Needleman et al. (1985). The plasticity theory pertinent to crystalline materials presented in the last reference is followed rather closely in this work. The first three subsections deal with the kinematics, the definition of an objective stress rate and the main features of crystal plasticity which are necessary in order to set up the numerical scheme presented in Section 3. The last subsection deals with crystal orientations and their evolution during the deformation process.

2.1. Kinematics

Consider a crystal occupying the domain Ω_O in the reference configuration κ_O where a crystallographic slip system is defined by the plane of normal $\mathbf{n}^{(s)}$ and by the direction of slip $\mathbf{m}^{(s)}$. Note that bold-face characters are used for vectors and tensors. The transformation convects the material to the current configuration κ_t where the solid occupies the domain Ω_t at time t. This transformation has a gradient, denoted by $\mathbf{F}(\mathbf{X}, t)$, at any point $\mathbf{x}$ in Ω_t which is occupied by a material particle found initially at $\mathbf{X}$ in Ω_O. During that transformation, any material vector of infinitesimal length $d\mathbf{X}$ is convected, stretched and rotated, and lies in the current configuration along the direction $d\mathbf{x}$ defined by $d\mathbf{x} = \mathbf{F} \cdot d\mathbf{X}$. The crystallographic slip direction $\mathbf{m}^{(s)}$ also sustains this convection as any material vector as long as no slip-system has been activated. Plastic shearing of the crystal does not however affect the slip systems orientation and thus it is the elastic part of the transformation which convects the slip direction once plasticity occurs.

This fundamental concept is accounted for with a multiplicative decomposition of the transformation gradient, proposed by Lee (1969)

$$\mathbf{F} = \mathbf{F}^e \cdot \mathbf{F}^p, \tag{1}$$

in terms of two gradients $\mathbf{F}^e$ and $\mathbf{F}^p$ where the latter is solely due to the plastic shearing resulting from the activation of the slip systems. The multiplicative decomposition of the transformation gradient expresses the composition of two transformations, the first from the reference to the intermediate configurations, the latter denoted $\Omega_{\mathrm{I}t}$ and the second transformation from the intermediate to the current configuration, as illustrated in Fig. 1. Complementary to the decomposition in (1), the normal and slip directions in the current configuration are thus determined solely by the elastic part of the transformation

$$\bar{\mathbf{m}}^{(s)} = \mathbf{F}^e \cdot \mathbf{m}^{(s)}, \quad \bar{\mathbf{n}}^{(s)} = \mathbf{n}^{(s)} \cdot \mathbf{F}^{e-1}. \tag{2}$$

The two vectors $\bar{\mathbf{m}}^{(s)}$ and $\bar{\mathbf{n}}^{(s)}$ are orthogonal but not unitary, a fact that will be discussed at a later stage. Starting from the rate form of (1), the Eulerian velocity gradient $\mathbf{L}$, which is equal to $\dot{\mathbf{F}} \cdot \mathbf{F}^{-1}$, is composed of two additive parts

$$\mathbf{L} = \mathbf{L}^e + \mathbf{L}^p,$$

with

$$\mathbf{L}^e = \dot{\mathbf{F}}^e \cdot \mathbf{F}^{e-1}, \quad \mathbf{L}^p = \mathbf{F}^e \cdot \mathbf{L}_{\mathrm{I}}^p \cdot \mathbf{F}^{e-1}, \tag{3}$$

and

$$\mathbf{L}_{\mathrm{I}}^p = \dot{\mathbf{F}}^p \cdot \mathbf{F}^{p-1}.$$

In (3), the tensor $\mathbf{L}_{\mathrm{I}}^p$ is the velocity gradient in the intermediate configuration which is defined in terms of the slip along the crystallographic systems as proposed by Rice (1971):

$$\mathbf{L}_{\mathrm{I}}^p = \sum_s \dot{\gamma}^{(s)} \mathscr{S}^{(s)} \quad \text{with } \mathscr{S}^{(s)} = \mathbf{m}^{(s)} \otimes \mathbf{n}^{(s)}, \tag{4}$$

in which the sum is over all activated slip systems, $\dot{\gamma}^{(s)}$ is the slip rate over the system s and the tensor $\mathscr{S}^{(s)}$ is the so-called Schmid tensor, in the intermediate (or reference) configuration, of the same slip system. Combining this assumption with the transformation (2) provides the following expression for the plastic part of the velocity gradient defined in (3)

$$\mathbf{L}^p = \sum_s \dot{\gamma}^{(s)} \bar{\mathscr{S}}^{(s)} \quad \text{with } \bar{\mathscr{S}}^{(s)} = \bar{\mathbf{m}}^{(s)} \otimes \bar{\mathbf{n}}^{(s)}, \tag{5}$$

in terms of the normal and the slip direction vectors in the current configuration with the introduction of the Schmid tensor $\bar{\mathscr{S}}^{(s)}$ in that configuration. The symmetric and the antisymmetric part of $\mathbf{L}^p$ are the plastic part of the rate of deformation tensor and of the spin tensor
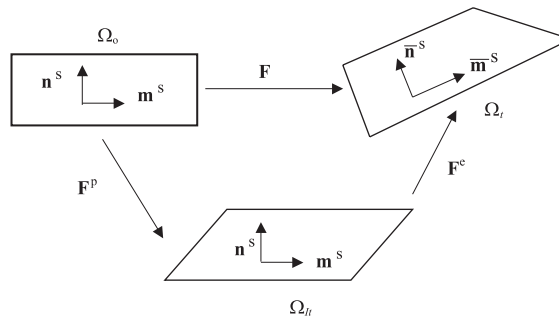

Fig. 1. Schematic of the decomposition of deformation into elastic and plastic parts, resulting in the relation, $\mathbf{F} = \mathbf{F}^e \cdot \mathbf{F}^p$.

$$\mathbf{D}^p = \sum_s \dot{\gamma}^{(s)} \mathbf{D}^{(s)} \quad \text{with } \mathbf{D}^{(s)} = \frac{1}{2}\left(\bar{\mathscr{S}}^{(s)} + {}^{\mathrm{T}}\bar{\mathscr{S}}^{(s)}\right),$$

$$\mathbf{W}^p = \sum_s \dot{\gamma}^{(s)} \mathbf{W}^{(s)} \quad \text{with } \mathbf{W}^{(s)} = \frac{1}{2}\left(\bar{\mathscr{S}}^{(s)} - {}^{\mathrm{T}}\bar{\mathscr{S}}^{(s)}\right),$$

(6)

which are defined in terms of $\mathbf{D}^{(s)}$ and $\mathbf{W}^{(s)}$, the symmetric and antisymmetric parts of the Schmid tensor in the current configuration, respectively. Note that in (6) the superscript T to the left of a tensor indicates its transpose. More specifically here,

$${}^{\mathrm{T}}\bar{\mathscr{S}}^{(s)} = \bar{\mathbf{n}}^{(s)} \otimes \bar{\mathbf{m}}^{(s)}.$$

(7)

The elastic parts of the rate of deformation and of the spin tensors are then simply defined from the symmetric and antisymmetric parts of (3a) using (6)

$$\mathbf{D}^e = \mathbf{D} - \mathbf{D}^p, \quad \mathbf{W}^e = \mathbf{W} - \mathbf{W}^p.$$

(8)

It should be stressed that the two definitions in (6) are central to the continuum theory of crystal plasticity.

2.2. Stress rate

The objective here is to define the time evolution of the Kirchhoff stress tensor in the current configuration in compliance with the principle of objectivity. The Kirchhoff stress τ is by definition $\det \mathbf{F}$ times the Cauchy stress. An objective stress rate $\overset{\nabla e}{\tau}$ is thus constructed for an observer attached to the crystal lattice. It is defined by

$$\overset{\nabla e}{\tau} = \dot{\tau} - \mathbf{W}^e \cdot \tau + \tau \cdot \mathbf{W}^e,$$

(9)

and has a structure identical to the classical Jaumann rate except that the spin tensor is solely due to the rotation of the lattice $\mathbf{W}^e$ defined in (8). It is this objective rate which enters the rate form of the constitutive relation

$$\overset{\nabla e}{\tau} = \mathscr{L}^e : \mathbf{D}^e,$$

(10)

in which $\mathscr{L}^e$ is the fourth-order elasticity tensor in the current configuration. It may be expressed in terms of the metric tensor $\mathbf{g}$ and in the case of isotropic elasticity, two scalar constants G and K the shear and bulk moduli respectively which are assumed to be independent of the state of deformation, resulting in an hypo-elasticity formulation. See Appendix A for an expression of the components of the elasticity tensor and note that the choice of isotropic elasticity could be amended to account for the elastic anisotropy of the crystals. Combining the definition of the stress rate in (9) with the decompositions in (8) and the definitions in (6) results in the following time derivative of the Kirchhoff stress

$$\dot{\tau} = \mathscr{L}^e : \mathbf{D} + \mathbf{W} \cdot \tau - \tau \cdot \mathbf{W} - \sum_s \dot{\gamma}^{(s)}\left(2G\mathbf{D}^{(s)} + \mathbf{P}^{(s)}\right),$$

$$\text{with } \mathbf{P}^{(s)} = \left(\mathbf{W}^{(s)} \cdot \tau - \tau \cdot \mathbf{W}^{(s)}\right).$$

(11)

This rate form of the constitutive response is now expressed as the difference between two terms, the first pertains to the elastic response of the material and the second involves plastic deformation by crystallographic slip (for details, see for example Asaro, 1983),

$$\dot{\tau} = \mathscr{T}_e(\mathbf{g}, \mathbf{D}, \tau) - \mathscr{T}_p\left(\dot{\gamma}^{(s)}, \tau, \mathbf{F}^p\right),$$

(12)

with

$$\mathscr{T}_e = \mathscr{L}^e : \mathbf{D} + \mathbf{W} \cdot \boldsymbol{\tau} - \boldsymbol{\tau} \cdot \mathbf{W},$$
$$\mathscr{T}_p = \sum_s \dot{\gamma}^{(s)} \big(2G\mathbf{D}^{(s)} + \mathbf{P}^{(s)}\big). \tag{13}$$

The component form of these constitutive relations is presented in Appendix A.

2.3. Slip activity

The mechanisms by which plastic deformation arises are linked to the activity of the slip systems. This activity is determined by the resolved shear stress over any system s, which is the scalar

$$\tau^{(s)} = \boldsymbol{\tau} : \mathbf{D}^{(s)}. \tag{14}$$

This quantity is the projection of the Kirchhoff stress tensor over the symmetric part of the Schmid tensor. This definition together with the definition of the plastic part of the rate of deformation tensor in (6) provides an interpretation of the slip rate $\dot{\gamma}^{(s)}$ as conjugate to the resolved shear stress in terms of the contribution of the system s to the total plastic power

$$\boldsymbol{\tau} : \mathbf{D}^p = \sum_s \dot{\gamma}^{(s)} \tau^{(s)}. \tag{15}$$

This construction justifies the choice of not normalizing the vectors $\bar{\mathbf{m}}^{(s)}$ and $\bar{\mathbf{n}}^{(s)}$ mentioned earlier. The next constitutive assumption is that each slip rate is a function of the resolved shear stress as well as a collection of internal variables which are denoted here as $\xi^{(s)}$ and could correspond to the slip system hardnesses, dislocation densities or any other parameters required to describe the evolution of the microstructure of the crystal. Both the slip rates and the rates of these internal variables have evolution laws of the type

$$\dot{\gamma}^{(s)} = \Gamma^{(s)}\Big(\tau^{(s)}, \xi^{(u)}\Big), \quad \dot{\xi}^{(s)} = \Xi^{(s)}\Big(\Gamma^{(u)}, \xi^{(u)}\Big). \tag{16}$$

The superscript u is used to identify the fact that systems other than s may enter the evolution law of that system. Specific choices are made in Section 4 to describe the rate-dependency and the evolution of hardening on slip systems for face-centered cubic crystals (fcc) but the generic forms in (16) are sufficient to motivate and discuss the proposed computational algorithm.

2.4. Crystal orientation and Schmid tensor

The initial orientation of a crystallite is given by the knowledge of the mapping from the base vectors $\{\mathbf{e}_j\}$ linked to the "laboratory" in the reference frame to a set of orthonormal base vectors $\mathbf{e}_j^c$ linked to crystallographic axes of the crystallite, which for cubic crystals are chosen as the "cubic" or $\langle 1\,0\,0 \rangle$ axes. This mapping is a rotation which defines the initial orientation matrix $\mathbf{Q}$ of the crystallite. The rotation $\mathbf{Q}$ is then $\mathbf{e}_i^c \otimes \mathbf{e}_i$ and its components in the laboratory axes are

$$Q_{ij} = \mathbf{e}_j^c \cdot \mathbf{e}_i. \tag{17}$$

The columns of the matrix $\mathbf{Q}$ are the components of the vectors $\mathbf{e}_i^c$ in the laboratory basis,

$$\mathbf{e}_i^c = Q_{ji}\mathbf{e}_j. \tag{18}$$

Equivalently, the initial orientation matrix may be constructed using Euler angles (e.g., Kalidindi et al., 1992; Kocks et al., 2000). In this case, the rows or columns of the initial orientation matrix may be interpreted as the crystallographic axes in the symmetric and Bunge conventions for the Euler angles, respectively.

In the reference configuration, the Schmid tensor for a slip system (s) has been defined in (4) as the cross product of the unit vectors $\mathbf{m}^{(s)}$ and $\mathbf{n}^{(s)}$ defining the glide direction and the slip plane normal. In the crystallographic (or cubic) axes, the components of these vectors, $m_i^{(s)C}$ and $n_i^{(s)C}$ respectively, are well known, with simple expressions directly linked to the Miller indices of the slip planes and directions (see Table 1 for the list of slip systems and corresponding Miller indices for fcc crystals). In the reference configuration, it is thus convenient to compute and store once and for all the components of the Schmid tensors in the crystallographic axes (notation, $\mathscr{S}_{ij}^{(s)C}$), and then use the orientation matrix $\mathbf{Q}$ in order to express these components in the "laboratory" axes (notation, $\mathscr{S}_{ij}^{(s)}$). More explicitely,

$$\mathscr{S}_{ij}^{(s)} = Q_{ip}\mathscr{S}_{pq}^{(s)C}Q_{jq}. \tag{19}$$

In the current configuration, the Schmid tensor remains defined by (5) and one has the relation:

$$\bar{\mathscr{S}}^{(s)} = \mathbf{F}^{\mathbf{e}} \cdot \mathscr{S}^{(s)} \cdot \mathbf{F}^{e-1}. \tag{20}$$

In crystal plasticity problems, the knowledge at any point in space and time of the current crystal orientation is most important since it amounts to the knowledge of the development of deformation textures. At any integration point, the current local orientation $\bar{\mathbf{Q}}$ follows from the integration of

$$\dot{\bar{\mathbf{Q}}} = \mathbf{W}^e\bar{\mathbf{Q}}. \tag{21}$$

An exact updating can be achieved with the assumption that $\mathbf{W}^e$ can be regarded as constant over the time interval Δt (see for instance Kocks et al., 2000),

$$\bar{\mathbf{Q}}_{t+\Delta t} = \mathrm{e}^{\mathbf{W}^e\Delta t}\mathbf{Q}_t. \tag{22}$$

The exponential of an antisymmetric second-order tensor is an orthogonal tensor that can be determined by the Rodrigues formula, so that,

$$\mathrm{e}^{\mathbf{W}^e\Delta t} = \mathbf{I} + \frac{\sin(w^e\Delta t)}{w^e}\mathbf{W}^e + \frac{1-\cos(w^e\Delta t)}{(w^e)^2}(\mathbf{W}^e)^2, \tag{23}$$

with $w^e = \sqrt{(W_{ij}^eW_{ij}^e)/2}$. This update will be implemented in the proposed scheme presented in the next section. It may be stressed already that $\bar{\mathbf{Q}}$ is computed at each integration point so that, owing to possibly nonuniform plastic deformation within a crystallite, an intracrystalline misorientation may arise.

Table 1
Schmid and Boas indexing of slip systems for fcc crystals

System name	Miller indices	
	Plane normal	Slip direction
A2	$(\bar{1}\,1\,1)$	$[0\,\bar{1}\,1]$
A3	$(\bar{1}\,1\,1)$	$[1\,0\,1]$
A6	$(\bar{1}\,1\,1)$	$[1\,1\,0]$
B2	$(1\,1\,1)$	$[0\,\bar{1}\,1]$
B4	$(1\,1\,1)$	$[\bar{1}\,0\,1]$
B5	$(1\,1\,1)$	$[\bar{1}\,1\,0]$
C1	$(\bar{1}\,\bar{1}\,1)$	$[0\,1\,1]$
C3	$(\bar{1}\,\bar{1}\,1)$	$[1\,0\,1]$
C5	$(\bar{1}\,\bar{1}\,1)$	$[\bar{1}\,1\,0]$
D1	$(1\,\bar{1}\,1)$	$[0\,1\,1]$
D4	$(1\,\bar{1}\,1)$	$[\bar{1}\,0\,1]$
D6	$(1\,\bar{1}\,1)$	$[1\,1\,0]$

3. Update algorithms and consistent linearization based on Runge–Kutta scheme

3.1. Rate equations and second-order Runge–Kutta method

The convected coordinates formalism adopted for the finite-element modeling is presented in Appendix A where the crystal plasticity theory outlined in the previous section is further discussed. The differential equations in rate form are summarized as follows,

$$
\begin{aligned}
\dot{\gamma}^{(s)} &= \Gamma^{(s)}\left(g_{ij}, F^P_{kl}, \tau^{mn}, \xi^{(u)}\right), \\
\dot{\xi}^{(s)} &= \Xi^{(s)}\left(\xi^{(u)}, \gamma^{(u)}\right), \\
\dot{F}^P_{ij} &= \mathscr{F}_{ij}\left(g_{kl}, F^P_{mn}, \dot{\gamma}^{(s)}\right), \\
\dot{\tau}^{ij} &= \mathscr{T}^{ij}_e(g_{kl}, D_{mn}, \tau^{rs}) - \mathscr{T}^{ij}_p\left(g_{kl}, D_{mn}, F^P_{rs}\right).
\end{aligned}
\tag{24}
$$

The first two equations are equivalent to (16) specifying as arguments in the first equation, the quantities necessary for the computation of the resolved shear stress, i.e. the covariant components of the metric tensor in the current configuration **g**, the nine components of the plastic part of the transformation gradient and the six components of the contravariant stress. The third equation corresponds to the definition of the plastic transformation gradient rate found from (3) and (4). The last of this set of equations corresponds to (12) with $\mathscr{T}^{ij}_e$ defining the stress rate in the absence of any slip and $\mathscr{T}^{ij}_p$ the plasticity correction to the previous stress rate due to the activation of the slip systems. If there is a total of N_s potential slip systems with N_i internal variables per system, then the set of equations (24) defines $15 + (N_i + 1) \times N_s$ equations to be integrated in time with appropriate initial conditions.

The complexity of this system calls for further simplifications of our notation with the hope to achieve a transparent presentation of the proposed algorithm. To this end, we define three sets of variables

$$
\begin{aligned}
z(t) &= \left(\frac{1}{2}g_{11}, \frac{1}{2}g_{22}, \frac{1}{2}g_{33}, g_{12}, g_{13}, g_{23} \middle| \frac{1}{2}D_{11}, \dots\right), \\
y_1 &= (\dots \gamma^s \dots), \\
y_2 &= \left(F^P_{11}, F^P_{21}, F^P_{31}, F^P_{12}, \dots \middle| \dots \xi^s \dots \middle| \tau^{11}, \tau^{22}, \tau^{33}, \tau^{12}, \dots\right).
\end{aligned}
\tag{25}
$$

The first set, z, has 12 components corresponding to the metric (**g**) and to the rate of deformation (**D**) covariant components which are seen here as being only functions of time. The second set is denoted y_1 and contains the accumulated slip on all the N_s crystallographic slip systems. The third set, y_2, contains the plastic part of the deformation gradient (F^P), the internal variables (ξ, e.g., hardening, dislocation density) and the contravariant stress (τ) components. The distinction made above between y_1 and y_2 becomes clear once system (24) is expressed in terms of the new variables

$$
\begin{aligned}
\dot{y}_1 &= Y_1(z(t), y_2), \\
\dot{y}_2 &= Y_2(z(t), Y_1, y_2).
\end{aligned}
\tag{26}
$$

The rate of the variable y_1, denoted Y_1, is an argument of the rate of the variable y_2, denoted Y_2, whereas y_1 does not contribute explicitly to Y_1.

After these preliminaries, we are now in position to discuss a family of update algorithms based on the Runge–Kutta (RK) method to integrate in time (26) as well as the linearization required to derive the consistent tangent operator for Newton–Raphson equilibrium search. The second-order scheme is

considered, again to simplify the presentation, and the reader is referred to Appendix C for a generalization to the fourth-order scheme. Time is discretized and the variables $y_\alpha (\alpha = 1, 2)$ are known at time n. The second-order Runge–Kutta scheme for the system of equations presented above consists of

$$
\begin{aligned}
& y_\alpha^{n+1} = y_\alpha^n + \frac{\Delta t}{2} \left(\overset{1}{Y}_\alpha + \overset{2}{Y}_\alpha \right), \quad \alpha = 1, 2, \\
& \overset{1}{Y}_1 = Y_1(z^n, y_2^n), \quad \overset{2}{Y}_1 = Y_1 \left(z^{n+1}, y_2^n + \Delta t \overset{1}{Y}_2 \right), \\
& \overset{1}{Y}_2 = Y_2 \left(z^n, \overset{1}{Y}_1{}^n, y_2^n \right), \quad \overset{2}{Y}_2 = Y_2 \left(z^{n+1}, \overset{2}{Y}_1, y_2^n + \Delta t \overset{1}{Y}_2 \right),
\end{aligned}
\tag{27}
$$

and provides the values of y_α after a time interval of Δt based on two estimates of the operators Y_α which are identified by the superposed number 1 and 2. The first estimate depends only on values at the beginning of the time step whereas the second depends on the rate of deformation tensor and the metric at the end of the time step as well as on the best estimate of the functions $\dot{y}_2$ and $\dot{y}_1$ to achieve a second-order accurate scheme. Note that the indices or superscripts n and $n + 1$ identify the time at which the variables are estimated.

The Runge–Kutta scheme has been used previously for the time integration of crystal plasticity constitutive equations in the rate form (e.g., Zikry, 1994). However, to the best of the authors' knowledge, the simplicity and accuracy afforded by this scheme has not been used previously to construct consistent tangent operators necessary for equilibrium search. The two variables which are directly functions of the nodal displacement obtained with a finite-element approximation are the metric and the rate of deformation tensor whose components are contained in the set z. It is the variation of the stress, with contravariant components contained in the set y_2, with respect to the set z which defines the consistent tangent first introduced by Simo and Taylor (1985). This consistent tangent is part of the operator relating the increment $\mathrm{d}y_2$ in response to an infinitesimal change in the set z denoted $\mathrm{d}z$ and is obtained by linearization of the algorithm. For the particular algorithm (27) of interest, one finds

$$
\mathrm{d}y_2 = \frac{\Delta t}{2} \left(\overset{2}{Y}_{2,z} + \overset{2}{Y}_{2,Y_1} \overset{2}{Y}_{1,z} \right) \mathrm{d}z,
\tag{28}
$$

in which a comma stands for partial differentiation with respect to the argument which follows. The linear operators $\overset{2}{Y}_{2,z}$, $\overset{2}{Y}_{2,Y_1}$ and $\overset{2}{Y}_{1,z}$ are matrices of dimension $(15 + N_\mathrm{i} \times N_\mathrm{s}) \times 12$, $(15 + N_\mathrm{i} \times N_\mathrm{s}) \times N_\mathrm{s}$ and $N_\mathrm{s} \times 12$, respectively (recall that N_s and N_i are the number of slip systems and of internal variables per system, respectively). Note that the first estimate $\overset{1}{Y}_\alpha$ does not depend on the values of the metric or the rate of deformation at the end of the time step, explaining the absence of its partial derivatives from the expression (28). The apparent simplicity of this result is certainly due to the choice of notation adopted here. It reveals that the consistent tangent implementation requires the partial derivatives of the operators Y_α defined in (26) which have to be estimated only once. The details of the expressions of these derivatives are given in Appendix B. The algorithm and methodology presented here can easily be adopted to other nonlinear constitutive models such as the von Mises (J_2) finite strain visco-plasticity or any other constitutive models if the evolution of the internal variables is given by first-order differential equations as, for example, in the case of shape memory alloys (Shaw et al., 2003).

3.2. Computational scheme

The computational procedure which has been implemented in the finite element code (SARPP, 2002) is now summarized for the case of the second-order Runge–Kutta scheme. The operations to be conducted

are grouped in three sets which are the initialization, the update and set-up of the local consistent tangent, and the global equilibrium search.

Set I: Initialization:
- Read material properties, number of slip systems N_s, Miller indices for each slip system and construct $\mathcal{S}_{pq}^{(s)C}$ (19) and initial crystal orientation $\mathbf{e}_1^c$ and $\mathbf{e}_2^c$.
- Compute tranverse direction $\mathbf{e}_3^c = \mathbf{e}_1^c \times \mathbf{e}_2^c$ in cubic axes and initial orientation matrix $\mathbf{Q}$ (17).
- Compute Schmid tensor $\mathcal{S}^{(s)}$ (12 for fcc) in reference laboratory frame (19).

Set II : Update and set-up of consistent tangent during iteration between t_n and t_{n+1}
- At element level (quadrature point), knowing at time t_n (G_{ij}^n, D_{ij}^n) compute current estimate $(G_{ij}^{n+1}, D_{ij}^{n+1})$ from current estimate of displacement field $\mathbf{u}^{n+1}$ at t_{n+1}.
- To prepare update of stress and other variables (y_1 and y_2) (25):

  > *For each of the two RK estimates, $k = 1, 2$:*
  - Compute elastic contribution to new stress $\mathcal{T}_e^{ij}$ (13 and A.10)
  - Compute inverse $\mathbf{F}^{p-1}$ from F_{ij}^p.
  - Compute hardening function (e.g.,34)

    $\triangledown$ *Loop over the N_s slip systems and for each:*
    - Compute $\bar{\mathcal{S}}_{kl}^{(s)}$, (5,A.8), $D_{kl}^{(s)}$ (6), $W_{kl}^{(s)}$ and $P^{(s)kl}$ (A.11).
    - Compute resolved shear stress $\tau^{(s)}$ (A.9) and check system activity.

      If system activated, otherwise consider next system
      - Compute $\dot{\xi}^{(s)}$ and $\dot{\gamma}^{(s)}$(16), part of $\overset{k}{Y}_1$ and $\overset{k}{Y}_2$.
      - Add contribution to the stress rate $\mathcal{T}_p^{ij}$ (13, A.11).
      - Add contribution to velocity gradient $\mathbf{L}_I^p$ (4).

    $\triangle$*End of loop over all slip systems.*

  - Complete setting of $\overset{k}{Y}_2$ and $\overset{k}{Y}_1$ with $\dot{F}_{kl}^p$ and $\mathcal{T}_p^{ij}$.
  - If $k = 2$, consistent tangent (28) set up according to Appendix B.
  $\triangleleft$ *End of RK loops*
- Update (intermediate or final) of stress and other variables (y_1 and y_2) with (27).

Set III: Assembly, equilibrium check and solve global system, if necessary,
- Perform global assembly of the element consistent stiffnesses and of the out-of-balance forces (obf).
- If norm of global obf less then *tol* (e.g., 10^{-6}) times maximum norm found over increment, convergence is achieved. Increment time and start next increment (Set II).
- If equilibrium not reached, solve for new estimate of displacement $\mathbf{u}^{n+1}$ and continue iterative process by repeating Set II for same time increment.

---

4. Crystalline slip and associated constitutive description

The new algorithm is illustrated through examples on deformation of face centered cubic (fcc) single crystals. It can be adapted for other types of crystals such as body centered cubic (bcc) or minerals such as

rock salt or calcite by introducing the appropriate definitions of the corresponding slip systems and hardening behavior.

4.1. Slip systems for fcc crystals

The fcc single crystal has 12 independent slip systems of the type $\{1\,1\,1\}\langle1\,1\,0\rangle$ and the Schmid–Boas convention for naming the slip systems is followed here, (see Table 1) with the choice made of a positive last index as in Franciosi and Zaoui (1982).

If one considers for instance system A2, in the reference cubic axes, the components of the unit slip direction vector and slip plane normal are respectively:

$$
\left(m_i^C\right) = \frac{1}{\sqrt{2}}\begin{pmatrix} 0 \\ -1 \\ 1 \end{pmatrix} \quad \text{and} \quad \left(n_i^C\right) = \frac{1}{\sqrt{3}}\begin{pmatrix} -1 \\ 1 \\ 1 \end{pmatrix}. \tag{29}
$$

4.2. Viscosity and hardening

For illustrative purposes, Schmid behavior or the applicability of critical resolved shear stress (CRSS) criterion for crystalline slip is assumed. NonSchmid behavior can be incorporated in the proposed algorithm without much difficulty. The specific forms of the shear strain rate and the hardening law (first two equations of (24)) are those employed by Needleman et al. (1985) in their computational modeling of rate dependent behavior of single crystals based on double slip. The viscoplastic behavior of the slip system is characterized by a power law relating the rate of shearing or slip on a given slip system $\left(\dot{\gamma}^{(s)}\right)$ to the resolved shear stress $\left(\tau^{(s)}\right)$ on the same system,

$$
\dot{\gamma}^{(s)} = \begin{cases} \dot{\gamma}_0 \quad \text{sign}\tau^{(s)}\left(\dfrac{\left|\tau^{(s)}\right|}{\tau_c^{(s)}}\right)^n & \text{if } \left|\tau^{(s)}\right| \geq \tau_c^{(s)}, \\ 0 & \text{otherwise}, \end{cases} \tag{30}
$$

where $\dot{\gamma}_0$ is a reference shear strain rate, $\tau_c^{(s)}$ is the current value of the CRSS and n is the strain rate sensitivity exponent. $n = \infty$ corresponds to the rate independent limit and $n = 1$ corresponds to that of a Newtonian fluid. The evolution of the CRSS on individual slip systems is given by a hardening law (Needleman et al., 1985),

$$
\dot{\tau}_c^{(\alpha)} = \sum_\beta h_{\alpha\beta}\left|\dot{\gamma}^{(\beta)}\right|, \tag{31}
$$

where $h_{\alpha\beta}(\gamma)$ are the self and latent hardening coefficients and are considered to be functions of the total accumulated slip (γ) on all the slip systems,

$$
\gamma = \int \sum_s \left|\dot{\gamma}^{(s)}\right|\mathrm{d}t, \tag{32}
$$

and the specific form the hardening coefficients used by Needleman et al. (1985) is adopted,

$$
h_{\alpha\beta} = \begin{cases} h & \text{if } \alpha = \beta, \\ qh & \alpha \neq \beta, \end{cases} \tag{33}
$$

where h is the self hardening coefficient for the diagonal terms and qh is the latent hardening coefficient for the off diagonal terms of the hardening matrix and

$$
h(\gamma) = h_0\mathrm{sech}^2\left(\frac{h_0\gamma}{\tau_* - \tau_0}\right), \tag{34}
$$

h_0 is a hardening proportionality constant, τ_* and τ_0 provide the saturation and reference shear stress on the slip system, defining the rate of hardening on individual slip systems. The parameter q which is the latent hardening ratio is assumed to be a constant, once again closely following Needleman et al. (1985). It seems realistic to apply the equations above to describe the behavior of fcc crystals at room temperature and small strain rates, although simpler or more complex approaches may also be easily implemented in the proposed algorithm for the shearing rate and hardening laws (e.g., Zarka, 1975; Franciosi et al., 1980; Cuitiño and Ortiz, 1992; Bassani, 1993; Delaire et al., 2000).

5. Illustrative examples

The second-order accurate Runge–Kutta method based scheme for crystal plasticity is initially applied to the modeling of single crystals, involving uniaxial tension and compression in various crystallographic directions, as well as simple shear along crystallographic directions. Finally, the newly developed algorithm is used in modeling strain localization which arises in a single crystal due to three-dimensional effects. In all the simulations, the same set of material properties are used unless otherwise mentioned and their values are tabulated in Table 2. The loading is applied along an axis whose projection on an inverse pole figure lies within the primary triangle bounded by directions, [0 0 1], [0 1 1] and [$\bar{1}$ 1 1] (see the [0 0 1] inverse pole figure projection shown in Fig. 2). For more details on inverse pole figures and the representations of a direction with respect to crystallographic axes, see for instance Bunge (1982) or Kocks et al. (2000).

Table 2
Material constants used in the simulations of fcc single crystals

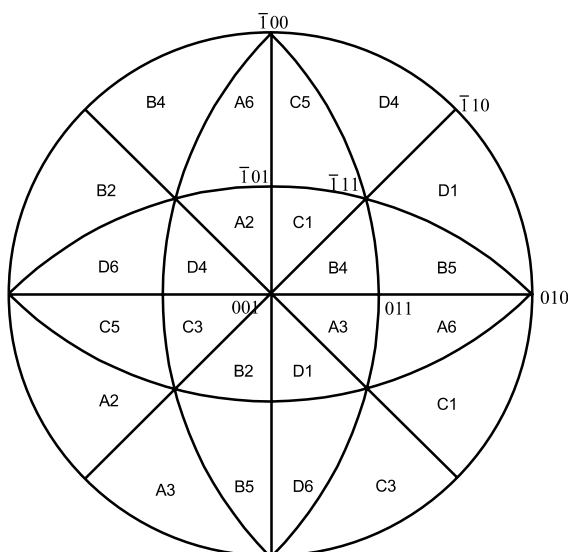| E_Y	v	$\dot{\gamma}_0$	n	τ_0	h_0/τ_0	τ_*/τ_0	q
1	0.3	10^{-3}	50	10^{-3}	8.9	1.8	1 or 1.4

Fig. 2. The [0 0 1] projection of the inverse pole figure plot for fcc single crystals (adapted from Franciosi and Zaoui (1982)).

5.1. Uniaxial tension and compression

To simulate uniaxial tension or compression on the crystal, a single 8-noded brick element of unit side is considered and is deformed at a constant specified displacement rate along X_2 axis of the reference frame. The two planes of the cube normal to the axis of loading are enforced to remain parallel to each other simulating a rigid testing machine. The single crystals were deformed along several crystallographic directions and the corresponding orthogonal initial crystallographic directions are given in Table 3. The crystals were deformed to a nominal strain of 0.5 at a strain rate of 1×10^{-3} s^{-1}. The data relating load–displacement, accumulated slip on active slip systems and as well as the rotation of the loading axis with respect to the cubic axes of the crystal are obtained from the simulations. The initial yield point and hence the yield stress and the active slip systems corresponding to each loading case are also listed in Table 3. In all the cases, for uniaxial loading, it is possible to determine the theoretical values for flow stress and as well as the accumulated slip, if one assumes a perfectly rigid rate independent plastic crystal. The analytical solution is given in Appendix D. The theoretically predicted values for flow stress, or the Taylor factor since $\sigma = M\tau_0$ and accumulated slip are listed in Table 3 for the nonhardening cases.

The crystals were loaded respectively along [0 0 1], [0 1 1] and [$\bar{1}$ 1 1], the corners of the primary triangle in the upper quadrant of the inverse pole figure (Fig. 2). In the nonhardening case ($h_0 = 0$), the crystals were stable in the initially specified orientation and equal slip on expected multiple slip systems (Fig. 2) was observed. The true stress–strain curves in tension are plotted for each case in Fig. 3(a) and accumulated slip on active slip systems is plotted in Fig. 3(b). Assuming the crystals to be rigid rate-independent plastic, the corresponding predicted flow stress and accumulated slip are also plotted on these figures. Despite the presence of elasticity and rate effects ($n = 50$), the discrepancy between the numerical and predicted is small ($\approx 2\%$). Similar features were also observed for compression along the above mentioned directions as shown in Fig. 4(a) and (b), where the simulations were performed for isotropic hardening for true strains of up to 0.25.

In order to investigate the ability of the numerical solution to capture features when rotations are involved, a crystal was subjected to tension along [$\bar{1}$ 2 3], the transverse axis being [5 4 $\bar{1}$] and the normal [1 $\bar{1}$ 1]. Several cases were considered, (i) no hardening, (ii) isotropic hardening with $q = 1$ and (iii) latent hardening with $q = 1.4$. In this case, the loading orientation is not stable and the crystal undergoes distortion in planes parallel to loading which results in rotation of the loading axis towards a stable orientation, namely the corners of the primary triangle in Fig. 2. The true stress–strain curves and accumulated slip as a function of strain for all the three cases mentioned above are plotted in Fig. 5(a) and (b). The corresponding path of the loading axis on the inverse pole figure (restricted to the primary triangle) is plotted in Fig. 5(c). Since the

Table 3
Directions of uniaxial loading in fcc single crystals and corresponding slip systems and Schmid factors for rate independent plasticity

Transverse axis x_1^c	Loading axis x_2^c	Normal axis x_3^c	Number $N^{(s)}$ and Name of active slip systems	Schmid factor S_0	Taylor factor M	Accumulated slip $\gamma^{(s)}/\epsilon$
[0 1 0]	[0 0 1]	[1 0 0]	8 A2 A3 B2 B4 C1 C3 D1 D4	0.408	2.45	0.306
[1 0 0]	[0 1 1]	[0 $\bar{1}$ 1]	4 A3 A6 B4 B5	0.408	2.45	0.612
[1 1 0]	[$\bar{1}$ 1 1]	[1 $\bar{1}$ 2]	6 B4 B5 C1 C5 D1 D4	0.272	3.67	0.612

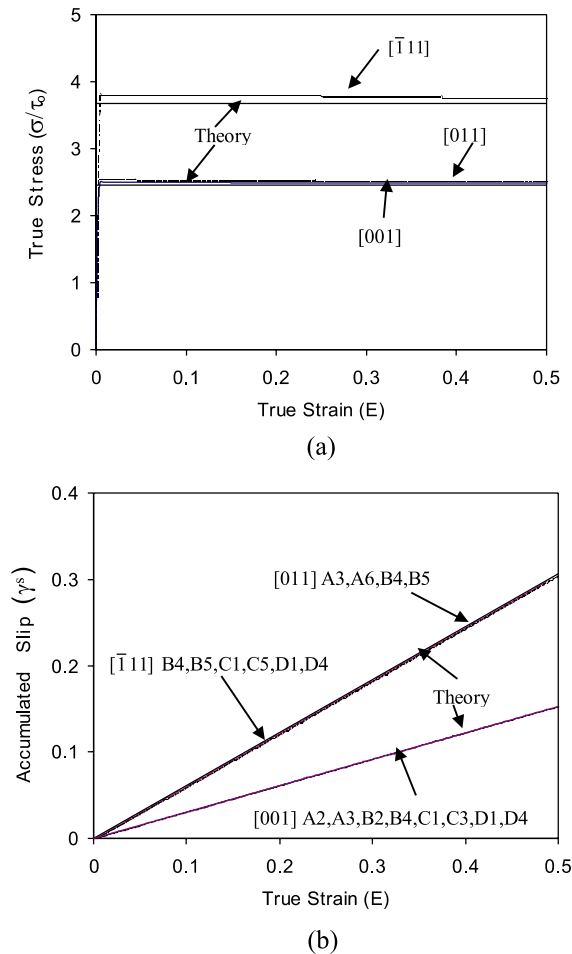Note: ϵ is the true strain, $M = \sigma/\tau_0 = 1/S_0$.

Fig. 3. Uniaxial tensile loading of fcc crystals along [0 0 1], [0 1 1] and [$\bar{1}$ 1 1] which are initially aligned with the X_2 axis of the reference frame: (a) true stress vs. true strain response and (b) accumulated slip vs. true strain on active slip systems indicated on the plot.

initial loading orientation lies within the primary triangle (Fig. 5(c)), the deformation induces single slip (primary) on slip system B4. As a result of single slip, one can observe parabolic hardening in the stress–strain curve even when the slip system has no inherent hardening, i.e., case (i). This is due to the geometrical effect of rotation induced by deformation. During deformation, the trajectory of the loading axis on the inverse pole figure follows a path moving away from its initial orientation [$\bar{1}$ 2 3] and towards the boundary of the primary triangle, namely, the [0 0 1]–[0 1 1] side. Upon reaching this side, secondary slip is induced on slip system C1. The two slip systems continue to accumulate slip at the same constant rate and the rate of accumulation of slip on the primary system B4 has decreased markedly indicated by the kink in the slip-strain curve for this system (Fig. 5(b)). Upon the activation of the secondary or conjugate slip, the loading axis on the inverse pole figure moves along the above mentioned side of the primary triangle towards [$\bar{1}$ 1 1], which is a stable orientation.

For the first two cases considered here, i.e., nonhardening and isotropic hardening ($q = 1$), though the stress–strain responses are markedly different, the history of accumulated slip on the two slip systems are
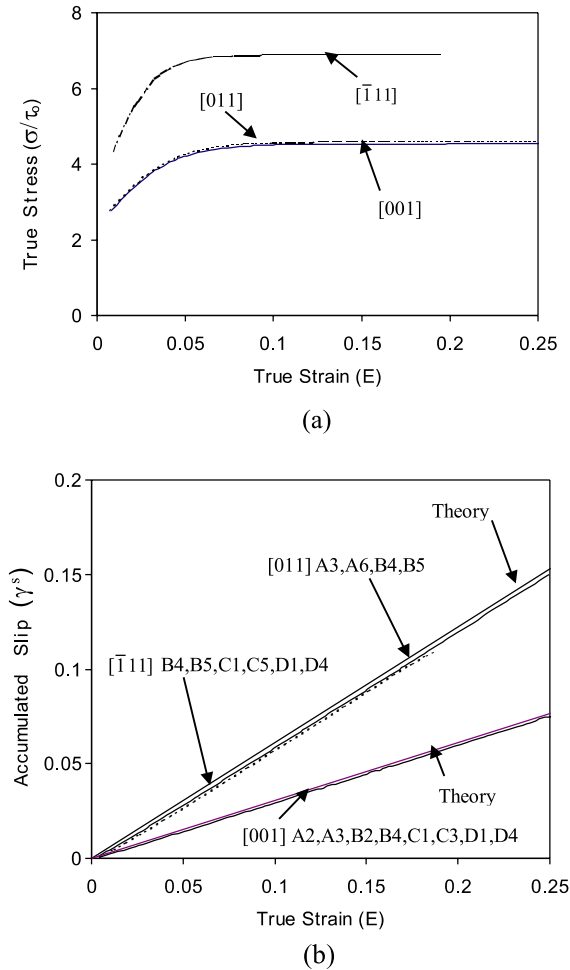
(a)

(b)

Fig. 4. Uniaxial compressive loading of fcc crystals along [0 0 1], [0 1 1] and [$\bar{1}$ 1 1] which are initially aligned with the X_2 axis of the reference frame: (a) true stress vs. true strain response and (b) accumulated slip vs. true strain on active slip systems indicated in the plot.

indistinguishable from each other (Fig. 5(b)), and, the same is true for the pole figures (Fig. 5(c)). This confirms that the accumulated slip is purely a function of deformation, in the absence of latent hardening effects. When one considers the last case involving latent hardening ($q = 1.4$), the response is markedly different for the stress–strain curve, which is to be expected. The onset of slip on the secondary slip system is delayed in comparison to the previous two cases involving isotropic hardening. Due to the delayed onset of the conjugate slip as a result of latent hardening, the pole figure path reveal the *overshoot* as indicated in Fig. 5(c), which crosses the tieline, and upon activation of the secondary slip, turns and follows a path nearly parallel to the [0 0 1]–[0 1 1] side, once again in the direction of the stable orientation [$\bar{1}$ 1 1]. Once secondary slip is activated, the rate of accumulated slip on the primary slip system decreases and both the slip systems accumulate at nearly the same constant rate. Similar observations were made by Anand and Kothari (1996) where they considered loading of an fcc crystal along [$\bar{2}$ 3 6], except that they report that the loading axis tends to become stable along the orientation [$\bar{1}$ 1 2] after a strain of 0.25.

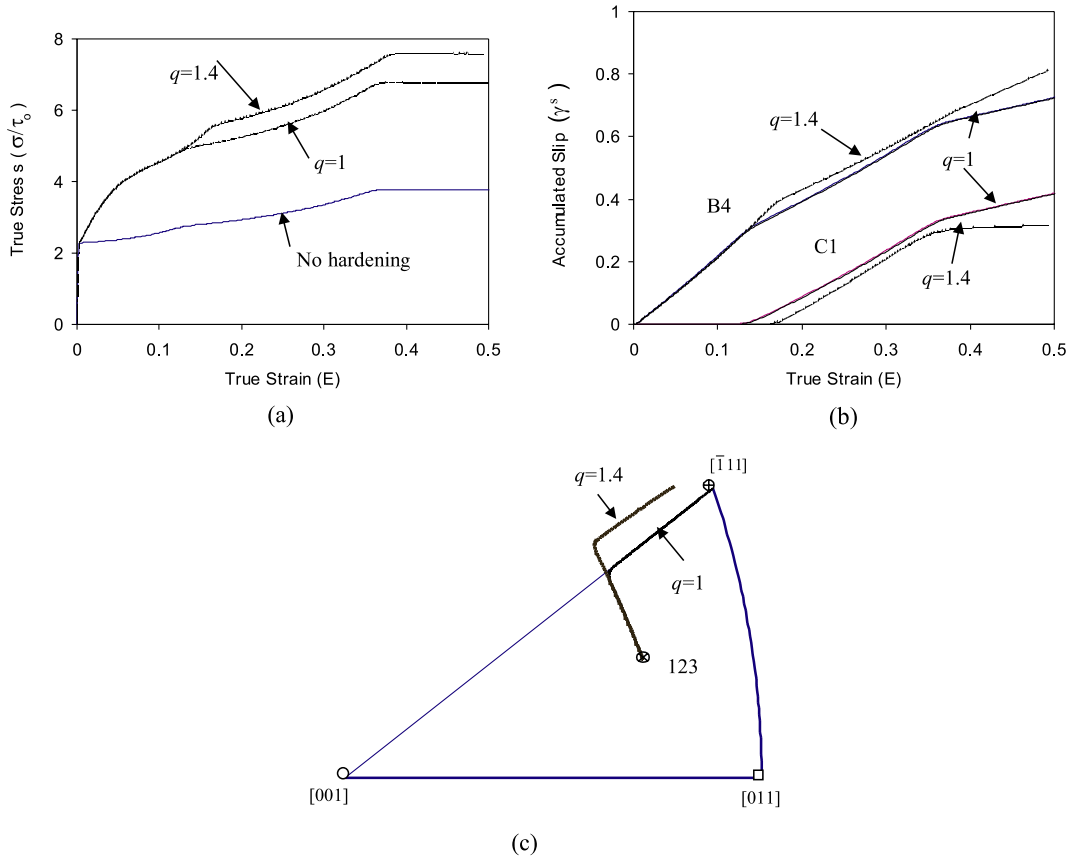(a)   (b)

(c)

Fig. 5. Uniaxial tensile loading of fcc crystal along $[\bar{1}\,2\,3]$ which is initially aligned with the X_2 axis of the reference frame: (a) true stress vs. true strain response; (b) accumulated slip vs. true strain on active slip systems marked on the plot and (c) path of pole figure projection of the loading axis in the standard triangle of the inverse pole figure.

In all the above mentioned simulations, the automatic time stepping scheme described in Section 3 was used. Generally the time step was around 0.1 for the values of rate sensitivity exponent and applied strain rate specified here. The corresponding tolerance in the norm of the increment for $\mathbf{F}^p$ used was 10^{-4}.

5.2. Simple shear

The fcc crystal was subjected to simple shear along $[1\,\bar{1}\,1]$ which is coincident with X_1 direction. The shearing was accomplished by constraining all the degrees of freedom in a single 8-noded brick element with unit side. The 4-nodes on the top surface were displaced in X_1 direction at a constant rate of 1×10^{-3} s^{-1}. Since all the displacements are specified, the computations become explicit, i.e., no iterations need to be performed for equilibrium check. The computations were performed for a time step of $\Delta t = 0.1$ and for shear strains of up to 2. The crystal remains in a state of plane strain and the lateral surfaces of the crystal remained traction free. The two sets of slip systems (A2, A3 and D1, D4) that are activated accumulate slip at differing rates. The shear stress–strain response of the crystal is shown in Fig. 6(a) and the accumulated slip on active slip systems are plotted in Fig. 6(b). The rotation of the slip system, which was tracked through the rotation of the normal to the shearing plane, i.e., $[\bar{1}\,1\,2]$, is plotted as a function of shear strain
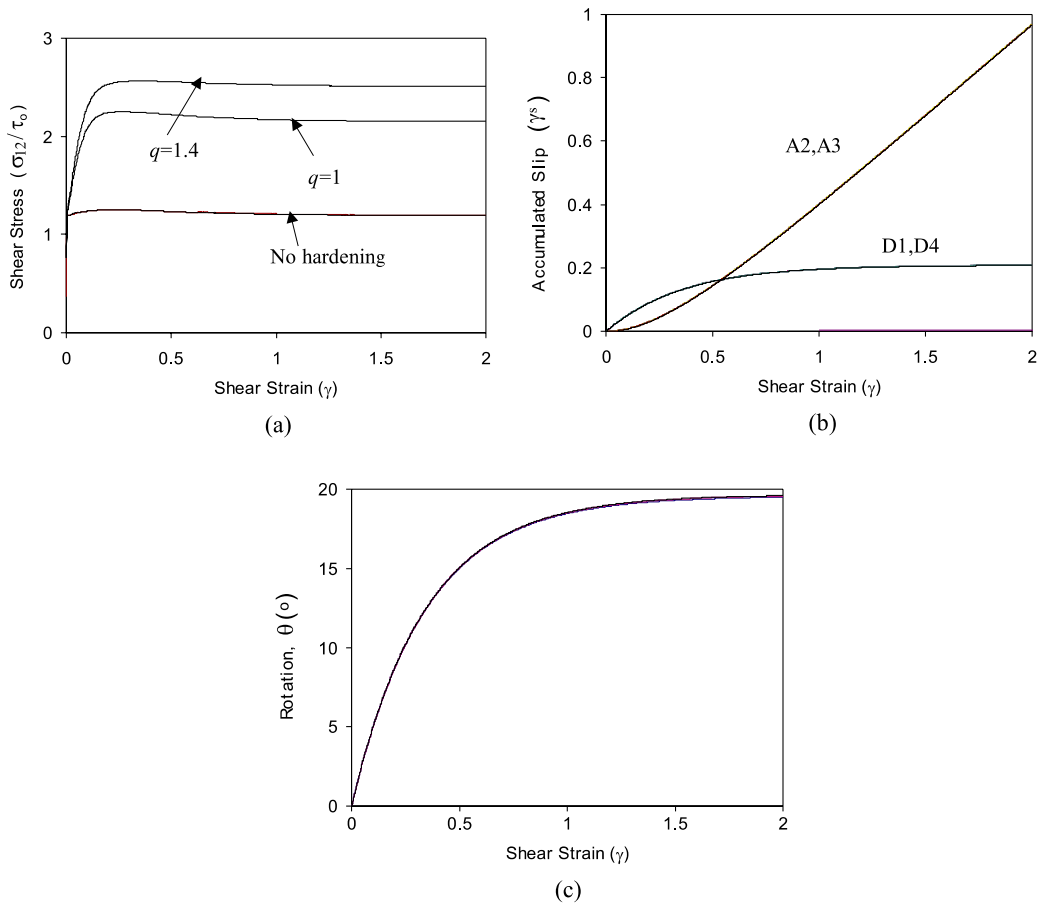
Fig. 6. Simple shearing of fcc crystal along [1 $\bar{1}$ 1] initially aligned with the X_1 axis of the reference frame: (a) shear stress vs. strain curves; (b) accumulated slip vs. shear strain curves and (c) rotation of the slip systems vs. shear strain.

in Fig. 6(c). The two sets of slip systems rotate by equal amounts. The slip systems are oriented along the glide direction $\langle 1\,1\,0 \rangle$ to the shear plane normal ([$\bar{1}\,1\,2$]) and the slip systems rotate in such a way so as to reach slip on a single glide system, i.e., the slip or glide planes become parallel to the shearing direction. The maximum rotation that leads to single slip is 19.47°, which is achieved after a shear strain of approximately 0.5. One can see that the slip on one set of slip systems (D1,D4) ceases to accumulate, leading to slip on a single system, (A2, A3). In all the cases, the shearing now occurs at a constant applied stress. The rotation of the slip system as a function of the shearing strain is found to be independent of the nature of hardening, i.e., independent of q.

Due to the finite deformation (Poynting like) effects, one also develops in-plane normal stresses, σ_{11} and σ_{22}, which are plotted in Fig. 7. These two stress components are of equal and of opposite sign, resulting in zero net hydrostatic pressure. These two components also change sign during the shearing deformation and this is due to the rotation of the two sets of slip systems. Similar results were shown for the double slip model by Miehe (1996). However, he observed an overshoot phenomenon in the shear stress response as a function of deformation, which was not observed in the current simulations, even in the case of anisotropic latent hardening, $q = 1.4$.
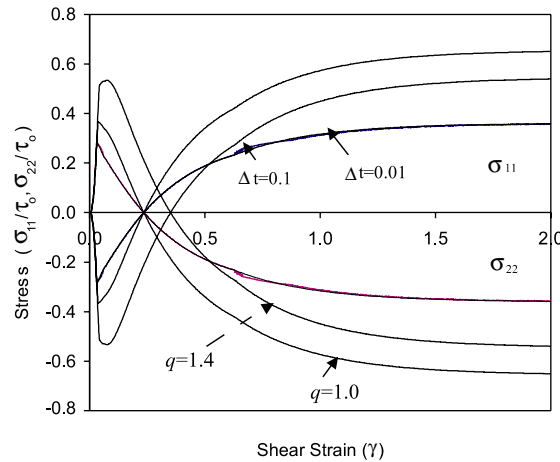
Fig. 7. Normal stress components (σ_{11} and σ_{22}) plotted as function of shear strain for no hardening and hardening with $q = 1.0$ and 1.4 for simple shearing of fcc crystal along [1 $\bar{1}$ 1] which is initially aligned with the X_1 axis of the reference frame.

In order to investigate the accuracy of the update in the numerical scheme, two different constant time steps were employed, $\Delta t = 0.01$ and 0.1, while keeping the rate sensitivity exponent and the deformation rate the same. The results of these simulations are also plotted in Fig. 7. Except in capturing relatively sharp changes during rotations, both time steps yield essentially the same results, which suggests that the present numerical update scheme is quite robust.

5.3. Onset of shear localization in 3D

In order to illustrate the full three-dimensional capabilities of the numerical algorithm, an example where localization could potentially occur is chosen. A single crystal of square cross section 4×4 mm and length of 25 mm, has been subjected to tension along x_2 which was made coincident with the crystallographic axis [$\bar{1}$ 1 2] while the transverse axes x_1 and x_3 were coincident with [1 1 0] and [1 $\bar{1}$ 1], respectively. This crystal has been used as the basis for developing the Asaro's double slip model (Asaro, 1979). The geometry and dimensions of the crystal are chosen to simulate the specimen used by Chang and Asaro (1981) in their investigation of localization in aluminum-copper single crystals.

Indeed, upon loading, slip occurs symmetrically on the two slip systems, namely, B4 and C1. The slip directions are and remain in the (1 $\bar{1}$ 1) plane (which is also the macroscopic plane (X_1, X_2)), each at 30° from the tensile axis. On the other free surface (X_2, X_3), parallel to the crystallographic plane (1 1 0), the slip plane traces are at 54° and 73° from the tensile axis. The crystallographic orientation is stable, which means that the crystallographic axes remain very close to their initial position with respect to the macroscopic axes.

The simulation has been performed using boundary conditions similar to the uniaxial loading with planes normal to the loading direction made to remain parallel. The bottom plane was restricted from moving in the loading direction but was free to move in the plane, except at one of the corners which was fixed in space to prevent rigid body motion and an additional point which was constrained to remain on macroscopic axis, in order to prevent rigid body rotations. No defect is initially present in the sample, contrary to what is extensively used as a seed for localization. The block is discretized into 6×38×6 for a total of 1368 uniform 27-noded brick elements and hence 13013 nodes. 27-noded elements were chosen to improve the accuracy and to be able to capture severe gradients that may occur in the deformation fields. The material properties that were used correspond to the isotropic hardening case ($q = 1$), and the strain
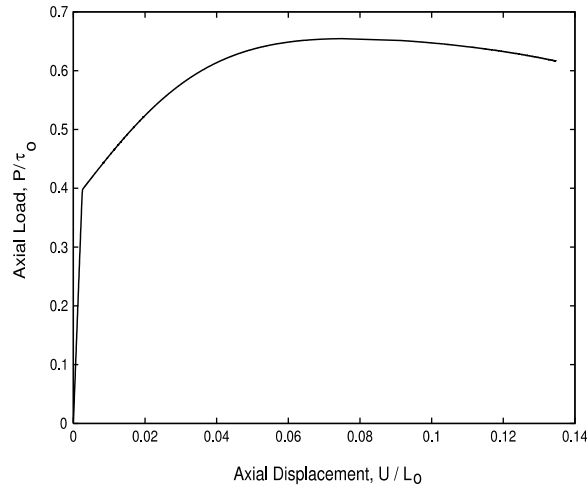
Fig. 8. Normalized axial load (P/τ_0) vs. normalized axial displacement (U/L_0) for the three-dimensional fcc single crystal block loaded along [$\bar{1}$12].
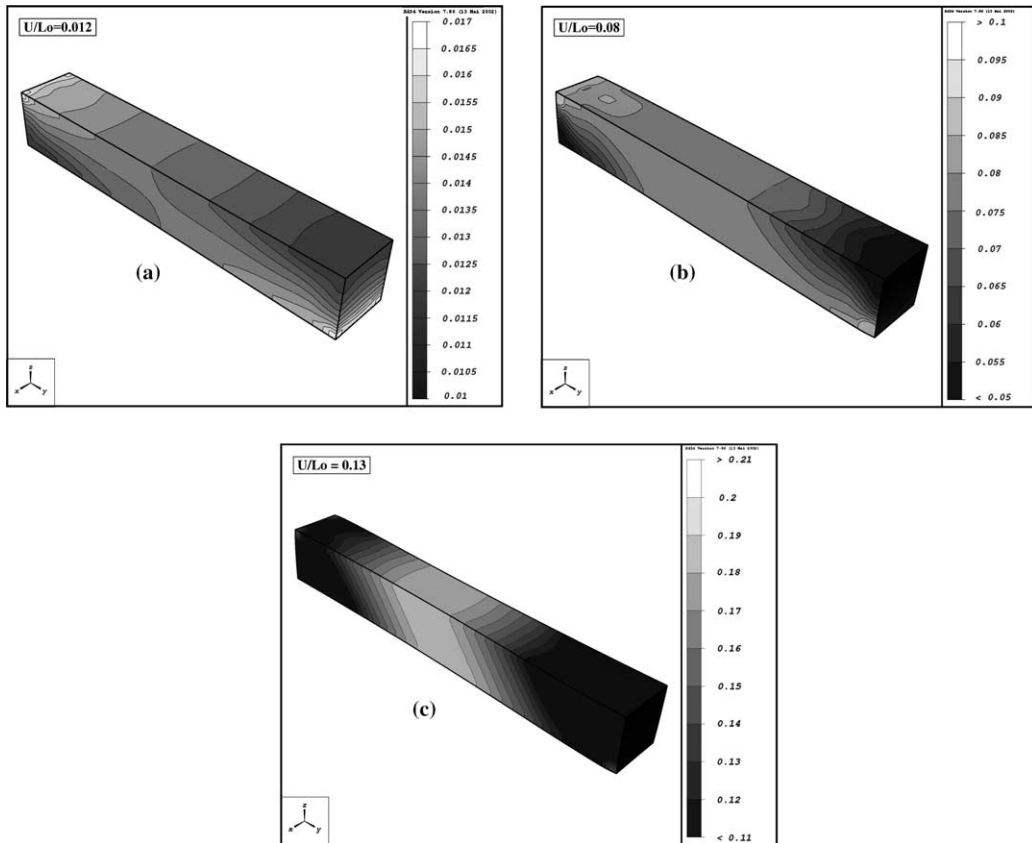

Fig. 9. Contours of axial strain E_{22} for the 3-D fcc single crystal block at various stages of deformation with corresponding normalized displacements, $U/L_0 = 0.012$ (a), 0.08 (b) and 0.13 (c).
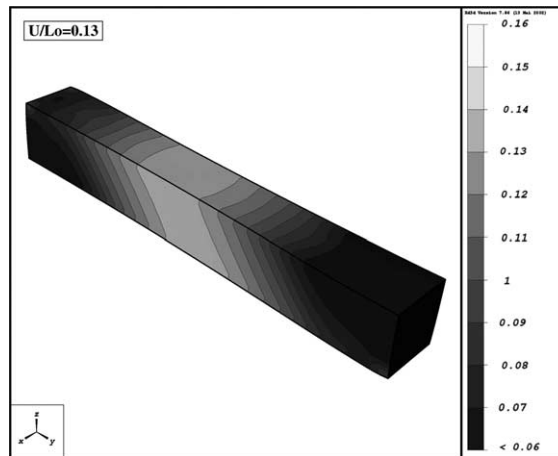
Fig. 10. Contours of shear strain E_{23} for the 3-D fcc single crystal block at a normalized displacement of $U/L_0 = 0.13$ at the early stages of localization.

rate sensitivity exponent, $n = 50$ was used. The elastic straining is homogeneous but the plastic response shows heterogeneous distributions of strains and stresses. This is to be expected since the ends of the samples are constrained to remain parallel to the plane (x_1, x_3) and this condition cannot be accommodated by plastic glide on the two prevailing systems over most of the sample, namely, B4 and C1. A local heterogeneous state of stress and strain is thus present near the ends and induces a local flexural type of deformation.

The load–displacement curve is plotted in Fig. 8, which shows the hardening followed by softening and eventually an abrupt drop in load, suggesting localization. This drop is not clearly seen on the figure itself. However, a very fast change of the orientation of the tangent to the load displacement curve happens, suggesting a very quick load drop, which in fact breaks down the computational procedure. The axial strain (E_{22}) at various stages of deformation is plotted in Fig. 9. Up to the maximum load corresponding to a normalized displacement (U/L_0) of 0.07, the deformation is fairly homogeneous. However beyond this point, the crystal clearly shows a tendency for shear localization in the transverse direction, see Fig. 9(c). The contours of shear strain (E_{23}) are plotted in Fig. 10 further revealing the localized nature of deformation. These results are in good qualitative agreement with the experimental observations of Chang and Asaro (1981). It is also worth stressing again here that the localization was induced even without the presence of a geometrical defect, which is necessary in 2D for creating asymmetry to induce localization.

6. Conclusion

A new algorithm for three-dimensional rate dependent crystal plasticity based on the Runge–Kutta integration scheme for system of partial differential governing equations is presented. The algorithm involves explicit constitutive update of the variables and the tangent has been derived based on consistent linearization of the governing equation for updating the Kirchhoff rate of stress. The stress update is based on an isotropic elastic predictor and plastic corrector, both of which are performed sequentially using the newly developed scheme. The algorithm has been implemented for the second-order Runge–Kutta scheme in a displacement based finite element code and the methodology for extending to the fourth-order scheme has been outlined. The consistent tangents are constructed at the element (local) level. Newton–Raphson iterative procedure is adopted for equilibrium check and quadratic rate of convergence is achieved. The

convergence in relative force norm of 10^{-6} is generally achieved in two iterations. The new algorithm provides a second-order accurate scheme, which provides higher order of accuracy than the current explicit schemes based on forward gradient methods and implicit schemes which use Euler schemes for integration of rate form of constitutive equations.

In the course of developing the algorithm, a methodology for computing crystal rotations without any assumptions regarding the magnitudes of elastic deformations or rotations is introduced. The new algorithm has been illustrated for one-dimensional loading (pure tension or compression and shear) of otherwise traction free 3D fcc single crystals loaded along crystallographic directions. The viscosity and hardening laws that were used are adopted from the works of Asaro, Needleman and coworkers. The simulations were performed on fcc single crystals and the material parameters that were used are also adopted from the above mentioned works (e.g., Needleman et al., 1985). When possible, the numerical solutions are compared with analytical results, which show excellent agreement, despite the elasticity. The scheme is capable of capturing the overshoot phenomena in crystals in the presence of latent hardening as demonstrated by the inverse pole figure plots for loading along an arbitrary crystallographic direction, such as $[\bar{1}\,2\,3]$. The ability of the numerical scheme to capture rotations of slip systems and as well as the effect of the size of increment on accuracy of the solution is demonstrated by subjecting the fcc single crystal to simple shear. As a final example, the three-dimensional capabilities of the numerical algorithm are demonstrated through the loading of a geometrically perfect fcc single crystal loaded along $[\bar{1}\,1\,2]$. Though the deformation in the loading plane is perfectly symmetric, the transverse shear provides the symmetry breaking mechanism, thus leading to localization.

The 3D crystal plasticity algorithm based on the Runge–Kutta integration scheme is demonstrated for fcc single crystals with isotropic elasticity and specific choice of viscosity and hardening laws. Since the consistent tangents are constructed at the element level, it is straightforward to include anisotropic elasticity, other choices of models for viscosity, evolution laws for hardening and as well as the number and crystallographic orientation of slip systems (e.g. bcc, rock salt). The order of accuracy of the Runge–Kutta update scheme can also be increased by implementing the fourth-order method discussed in Appendix C.

Acknowledgements

Appendix A. Convected coordinates formulation for crystal plasticity

The convected coordinate formalism is adopted for the finite-element implementation of crystal plasticity in the context of finite deformation. A concise presentation of this formalism is found in Needleman et al. (1985), which is used in the next two sections, the first one dealing with kinematics and the second with the definition of stress and stress rates.

A.1. Kinematics

The initial unstressed configuration is taken to be the reference configuration, where the position of a material point is given by $\mathbf{X}(\chi^i, t)$ in terms the material coordinates χ^i. After transformation, the material

point is at $\mathbf{x}(\chi^i, t)$ in the current configuration. All the field quantities are thus considered to be functions of the convected coordinates, χ^i, which serve as particle labels, and time t. The covariant base vectors $\mathbf{G}_i$ and $\mathbf{g}_i$ in the reference and current configuration are

$$\mathbf{G}_i = \frac{\partial \mathbf{X}}{\partial \chi^i}, \quad \mathbf{g}_i = \frac{\partial \mathbf{x}}{\partial \chi^i}, \tag{A.1}$$

respectively. The contravariant base vectors are obtained from the following orthogonality conditions

$$\mathbf{G}_i \cdot \mathbf{G}^j = \delta_i^j = \mathbf{g}_i \cdot \mathbf{g}^j, \tag{A.2}$$

and the metric tensors are defined by

$$\Delta = \mathbf{G}_i \otimes \mathbf{G}^i = G_{ij}\mathbf{G}^i \otimes \mathbf{G}^j, \quad \mathbf{g} = \mathbf{g}_i \otimes \mathbf{g}^i = g_{ij}\mathbf{g}^i \otimes \mathbf{g}^j, \tag{A.3}$$

where G_{ij} and g_{ij} are the covariant components of the metric tensors Δ and $\mathbf{g}$ in the reference and current configuration, respectively. Any material vector of infinitesimal length $\mathrm{d}\mathbf{X} = \mathrm{d}\chi^i\mathbf{G}_i$ at $\mathbf{X}$ is convected to the vector $\mathrm{d}\mathbf{x} = \mathrm{d}\chi^i\mathbf{g}_i$ found at $\mathbf{x}$ in the current configuration so that the transformation gradient $\mathbf{F}$, which relates the two vectors by $\mathrm{d}\mathbf{x} = \mathbf{F} \cdot \mathrm{d}\mathbf{X}$, and its inverse $\mathbf{F}^{-1}$ are

$$\mathbf{F} = \mathbf{g}_i \otimes \mathbf{G}^i, \quad \mathbf{F}^{-1} = \mathbf{G}_i \otimes \mathbf{g}^i. \tag{A.4}$$

The Lagrangian strain tensor $\mathbf{E}$ is defined as

$$\mathbf{E} = \frac{1}{2}(\mathbf{F}^t \cdot \mathbf{F} - \Delta) = \frac{1}{2}(g_{ij} - G_{ij})\mathbf{G}^i \otimes \mathbf{G}^j, \tag{A.5}$$

and its components are half the difference between the components of the two metric tensors defined above. The plastic part of the transformation gradient $\mathbf{F}^p$ and its inverse $\mathbf{F}^{p-1}$ are defined in the reference configuration as

$$\mathbf{F}^p = F^{pij}\mathbf{G}_i \otimes \mathbf{G}_j, \quad \mathbf{F}^{p-1} = F^{p-1ij}\mathbf{G}_i \otimes \mathbf{G}_j. \tag{A.6}$$

Making use of the multiplicative decomposition of the transformation gradient $\mathbf{F}$ in (1), the elastic part of the transformation gradient $\mathbf{F}^e$ and its inverse $\mathbf{F}^{e-1}$ are then written as,

$$\begin{aligned} \mathbf{F}^e &= \mathbf{F} \cdot \mathbf{F}^{p-1} = F^{p-1kl}\mathbf{g}_k \otimes \mathbf{G}_l, \\ \mathbf{F}^{e-1} &= \mathbf{F}^p \cdot \mathbf{F}^{-1} = F_l^{pk}\mathbf{G}_k \otimes \mathbf{g}^l, \end{aligned} \tag{A.7}$$

where the rule $F_l^{pk} = F^{pki}G_{il}$ for lowering indices and resulting in mixed components has been applied.

These preliminaries are now put into use for expressing the components of the Schmid tensor in the current configuration. For that purpose start from the definition (5) and apply the transformation of the normal and slip directions in (2)

$$\bar{\mathscr{S}}^{(s)} = \mathbf{F}^e \cdot \mathscr{S}^{(s)} \cdot \mathbf{F}^{e-1} = \left(F^{p-1pi}\mathscr{S}_{ij}^{(s)}F^{pjl}\right)\mathbf{g}_p \otimes \mathbf{g}_l. \tag{A.8}$$

A.2. Stress

The resolved shear stress, defined in (14), is now expressed as

$$\tau^s = \tau^{ij}D_{ij}^{(s)}, \tag{A.9}$$

where τ^{ij} are the components of the Kirchhoff stress in the current configuration and $D_{ij}^{(s)}$ the covariant components of the symmetric part of Schmid tensor obtained with the rule for lowering indices from the contrariant component of the Schmid tensor defined in (A.8).

The time rate of Kirchhoff stress defined in (12) has been decomposed as the difference between an elastic and a plastic terms which components are now introduced as

$$\mathscr{T}_e^{ij} = \big(\mathscr{L}_e^{ijkl} - \mathscr{M}^{ijkl}\big)D_{kl}, \tag{A.10}$$

with

$$\mathscr{L}^{eijkl} = \left(K - \frac{2G}{3}\right)g^{ij}g^{kl} + G\big(g^{ik}g^{lj} + g^{il}g^{kj}\big),$$

$$\mathscr{M}^{ijkl} = \frac{1}{2}\big(g^{ik}\tau^{lj} + g^{il}\tau^{kj} + g^{jk}\tau^{li} + g^{jl}\tau^{ki}\big).$$

and

$$\mathscr{T}_p^{ij} = \sum_s \dot{\gamma}^{(s)}\big(2GD^{(s)ij} + P^{(s)ij}\big), \tag{A.11}$$

with

$$P^{(s)ij} = W_{kl}^{(s)}\big(\tau^{lj}g^{ki} + \tau^{ki}g^{lj}\big),$$

$$W_{kl}^{(s)} = \frac{1}{2}\left(\bar{\mathscr{S}}_{kl}^{(s)} - \bar{\mathscr{S}}_{lk}^{(s)}\right).$$

Appendix B. Consistent tangent for the second-order Runge–Kutta algorithm

The objective of this Appendix B is to provide the details of the operators which enters the consistent tangent (28) and are necessary for the numerical implementation. As mentioned earlier, it is only part of the expression (28) which is needed to form the consistent tangent between the components of the Kirchhoff stress and of the Lagrangian deformation tensor and the rate of deformation tensor. Using a matrix notation consistent with Section 3 of this paper, that substructure of (28) is

$$\{d\tau^{ij}\} = \frac{\Delta t}{2}\left(\left[\frac{\partial \mathscr{T}_e^{ij}}{\partial E_{kl}} - \frac{\partial \mathscr{T}_p^{ij}}{\partial E_{kl}}\bigg| \frac{\partial \mathscr{T}_e^{ij}}{\partial D_{kl}} - \frac{\partial \mathscr{T}_p^{ij}}{\partial D_{kl}}\right] - \left[\sum_s \frac{\partial \mathscr{T}_p^{ij}}{\partial \dot{\gamma}_s}\frac{\partial \dot{\gamma}_s}{\partial E_{kl}}\bigg| \sum_s \frac{\partial \mathscr{T}_p^{ij}}{\partial \dot{\gamma}_s}\frac{\partial \dot{\gamma}_s}{\partial D_{kl}}\right]\right)\left\{\begin{array}{c} dE_{kl} \\ dD_{kl} \end{array}\right\}. \tag{B.1}$$

In that equation, the partition of the stress rate in the two operators defined in (12) has been already accounted for. The linearization of stress rates in component form (A.10) with respect to the metric and the rate of deformation components provides

$$\frac{\partial \mathscr{T}_e^{ij}}{\partial E_{kl}} = -\left(K - \frac{2G}{3}\right)\big(g^{ik}g^{jl}g^{pq}D_{pq} + g^{ij}D^{kl}\big) - 2G\big(g^{ik}D^{lj} + g^{jl}D^{ik} + g^{ik}D^{jl} + g^{jl}D^{ki}\big)$$
$$+ g^{ik}\big(D_q^l\tau^{qj} + D_q^l\tau^{qj}\big) + g^{jk}\big(D_q^l\tau^{qi} + D_q^l\tau^{pi}\big), \tag{B.2}$$

$$\frac{\partial \mathscr{T}_e^{ij}}{\partial D_{kl}} = \mathscr{L}_e^{ijkl} - \mathscr{M}^{ijkl},$$

for the elastic part. The plastic contribution to the stress rate is found in (A.11) and its differentiation with respect to the kinematical variables provides

$$\frac{\partial \mathcal{T}_p^{ij}}{\partial E_{kl}} = 2W^{(s)kn}g_{nb}\left(\tau^{bj}g^{li} + \tau^{li}g^{bj}\right) + 2W^{(s)mk}g_{ma}\left(\tau^{lj}g^{ai} + \tau^{ai}g^{lj}\right)$$
$$- 2W_{ab}^{(s)}(\tau^{bj}g^{ak}g^{il} + \tau^{ai}g^{bk}g^{jl}), \tag{B.3}$$

$$\frac{\partial \mathcal{T}_p^{ij}}{\partial D_{kl}} = 0.$$

The last items of interest here are the partial derivatives of the plastic contribution to the stress rate with respect to the slip strain rate

$$\frac{\partial \mathcal{T}_p^{ij}}{\partial \dot{\gamma}^s} = 2GD^{(s)ij} + P^{(s)ij}, \tag{B.4}$$

and the partial derivatives of the slip strain rate with respect to the kinematical variables

$$\frac{\partial \dot{\gamma}_s}{\partial E_{kl}} = \frac{\partial \Gamma_s}{\partial E_{kl}}, \quad \frac{\partial \dot{\gamma}_s}{\partial D_{kl}} = 0. \tag{B.5}$$

Note that the right-hand side of (B.3a) should be symmetrized for preserving the symmetries of the stress and strain and that the partial derivatives of the slip law with respect to the Lagrangian strain components (B.5a) depend on the specifics of the model selected and are not discussed further here. Results in (B.2)–(B.5) can now be combined in (B.1) to provide the consistent tangent, a task left for the numerical implementation.

Appendix C. Fourth-order Runge–Kutta update algorithm

The update and consistent linearization of the system of equations in (26) for the fourth-order Runge–Kutta algorithm is now presented. The update scheme reads

$$y_\alpha^{n+1} = y_\alpha^n + \frac{\Delta t}{6}\left[\overset{1}{Y}_\alpha + 2\left(\overset{2}{Y}_\alpha + \overset{3}{Y}_\alpha\right) + \overset{4}{Y}_\alpha\right], \quad \alpha = 1, 2,$$

$$\overset{1}{Y}_1 = Y_1(z^n, y_2^n), \quad \overset{2}{Y}_1 = Y_1\left(z^{n+\frac{1}{2}}, y_2^n + \frac{\Delta t}{2}\overset{1}{Y}_2\right),$$

$$\overset{3}{Y}_1 = Y_1\left(z^{n+\frac{1}{2}}, y_2^n + \frac{\Delta t}{2}\overset{2}{Y}_2\right), \quad \overset{4}{Y}_1 = Y_1(z^{n+1}, y_2^n + \Delta t\overset{3}{Y}_2),$$

$$\overset{1}{Y}_2 = Y_2\left(z^n, \overset{1}{Y}_1^n, y_2^n\right), \quad \overset{2}{Y}_2 = Y_2\left(z^{n+\frac{1}{2}}, \overset{2}{Y}_1, y_2^n + \frac{\Delta t}{2}\overset{1}{Y}_2\right), \tag{C.1}$$

$$\overset{3}{Y}_2 = Y_2\left(z^{n+\frac{1}{2}}, \overset{3}{Y}_1, y_2^n + \frac{\Delta t}{2}\overset{2}{Y}_2\right),$$

$$\overset{4}{Y}_2 = Y_2(z^{n+1}, \overset{4}{Y}_1, y_2^n + \Delta t\overset{3}{Y}_2),$$

where

$$z^{n+\frac{1}{2}} = \frac{1}{2}(z^n + z^{n+1}). \tag{C.2}$$

These equations provide the values of y_α after a time interval of Δt at time $n + 1$ based on the four estimates of the operators $\overset{k}{Y}_\alpha$ which are identified by the superposed numbers 1–4 corresponding to the Runge–Kutta steps. The first step depends only on values at the beginning of the time step whereas the fourth depends on the rate of deformation tensor and the metric at the end of the time step as well as on the optimum estimate

of the variable $\dot{y}_2$ and y_1 to achieve a fourth-order accurate scheme. The second and third steps depend on the intermediate value of the vector z. Note that the superscripts n, $n + 1/2$ and $n + 1$ identify the times at which the variables are estimated.

Similar to the second-order accurate scheme, the consistent tangent is part of the operator relating the increment dy_2 in response to an infinitesimal change in the set z denoted dz and is obtained by linearization of the algorithm. The first step of this consistent tangent derivation is thus the linearization of the four estimates $\overset{k}{Y}_2$

$$
d\overset{1}{Y}_2 = 0, \quad d\overset{2}{Y}_2 = \frac{1}{2}\overset{2}{F}_2\, dz,
$$
$$
d\overset{3}{Y}_2 = \frac{1}{2}\overset{3}{F}_2\, dz + \frac{\Delta t}{2}\overset{3}{R}_2 d\overset{2}{Y}_2,
$$
$$
d\overset{4}{Y}_2 = \overset{4}{F}_2\, dz + \Delta t \overset{4}{R}_2\, d\overset{3}{Y}_2,
$$
(C.3)

in which the following notation has been adopted to make a compact presentation

$$
\overset{k}{F}_2 = \overset{k}{Y}_{2,z} + \overset{k}{Y}_{2,Y_1}\overset{k}{Y}_{1,z}, \quad \overset{k}{R}_2 = \overset{k}{Y}_{2,y_2} + \overset{k}{Y}_{2,Y_1}\overset{k}{Y}_{1,y_2},
$$
(C.4)

where k denotes the Runge–Kutta step (1–4) at which the expressions are evaluated. The matrices $\overset{k}{F}_2$ and $\overset{k}{R}_2$ have for dimension $(15 + N_s \times N_i) \times 12$ and $(15 + N_s \times N_i) \times (15 + N_s \times N_i)$, respectively (recall that N_s and N_i are the number of slip system and the number of internal variables per system) The second step of the linearization consists of combining the results in (C.3) according to the linearized version of (C.1a) ($\alpha = 2$) to obtain the operator which includes the consistent tangent

$$
dy_2 = \frac{\Delta t}{6}\left[\overset{2}{F}_2 + \overset{4}{F}_2 + \left(I + \frac{\Delta t}{2}\overset{4}{R}_2\right)\left(\overset{3}{F}_2 + \frac{\Delta t}{2}\overset{3}{R}_2\overset{2}{F}_2\right)\right] dz,
$$
(C.5)

in which I is the identity matrix of same dimension as $\overset{k}{R}_2$. Note that the operators and their derivatives defined for the second-order scheme enter the fourth-order scheme (except for $\overset{k}{R}_2$) and thus a generalization from the former to the latter offers no difficulty.

Appendix D. Uniaxial loading of a rate independent rigid plastic fcc single crystal

The procedure for determining the flow stress, active slip systems and accumulated slip on these systems due to uniaxial loading is well established (see for example, Reid (1972)) and the results are summarized here for the sake of completeness.

Consider the deformation of a rate-independent rigid plastic crystal that is subjected to deformation along a certain direction at a constant nominal strain rate, for example, $\dot{\epsilon}_{22} = \dot{\epsilon}$. The nominal strain rate is related to the true strain rate, $\dot{E} = \dot{\epsilon}/(1 + \epsilon)$. This results in a stress state corresponding to, $\sigma_{22} = \sigma$ and all other $\sigma_{ij} = 0$. The order and number of slip systems that will be activated depends on the crystal orientation and the Schmid factor. In the present case, the slip systems that are favorably oriented, i.e., the ones that have the highest Schmid factor, S, ($\bar{m}_2\bar{n}_2$ in the reference frame) will be first activated. If the crystal does undergo rotations during deformation, additional slip systems may be activated or the slip systems currently undergoing slip may cease to be active. First we consider the cases, where there is no rotation of the crystal lattice, in which case the Schmid factor will remain a constant at its initial value S_0 throughout the deformation. This situation arises when the highest Schmid factor is initially the same on an even number of slip systems, which we denote here by $\mathcal{N}$.

Let us assume that the critical resolved shear stress to be the same for all slip systems, τ_{c0}, which remains a constant in the absence of hardening. When slip initiates, the crystal continues to deform at a constant true stress given by,

$$\sigma = \frac{\tau_{c0}}{S_0} = M\tau_{c0}, \tag{D.1}$$

where M is the Taylor factor $(1/S_0)$ The imposed deformation is accommodated by slip on the glide planes,

$$\dot{E} = \sum_{s=1}^{s=\mathcal{N}} \dot{\gamma}^s S_0 = \mathcal{N} S_0 \dot{\gamma}^s, \tag{D.2}$$

where $\dot{\gamma}^s$ is the slip rate on each slip system and in the present case they all are identical, hence,

$$\dot{\gamma}^s = \frac{M\dot{E}}{\mathcal{N}}, \quad \gamma^s = \frac{ME}{\mathcal{N}}. \tag{D.3}$$

The relations (D.1) and (D.3) contain the necessary information to completely characterize the response of the crystal to uniaxial loading. The Schmid factors, S_0, for deformation along [0 0 1], [0 1 1] and [$\bar{1}$ 1 1] directions are $\frac{1}{\sqrt{6}}$, $\frac{1}{\sqrt{6}}$ and $\frac{\sqrt{2}}{3\sqrt{3}}$, respectively. The corresponding number of slip systems, $\mathcal{N}$ on which equal amount of slip accumulates are 8, 4 and 6, respectively (Fig. 2).

References

Anand, L., Kothari, M., 1996. A computational procedure for rate-independent crystal plasticity. J. Mech. Phys. Solids. 44, 525–558.

Asaro, R.J., 1979. Geometric effects in the inhomogeneous deformation of ductile single crystals. Acta Metall. 27, 445–453.

Asaro, R.J., 1983. Micromechanics of crystals and polycrystals. Adv. Appl. Mech. 23, 1–115.

Asaro, R.J., Rice, J.R., 1977. Strain localization in ductile single crystals. J. Mech. Phys. Solids 25, 309–338.

Bassani, J.L., 1993. Plastic flow of crystals. Adv. Appl. Mech. 30, 191–258.

Bunge, H., 1982. Texture: general outline. Series expansion method. In: Bunge, H., Esling, C. (Eds.), Quantitative Texture Analysis Deutsche Gesellschaft für Metallkunde. pp. 1–70.

Chang, Y.W., Asaro, R.J., 1981. An experimental study of shear localization in aluminum-copper single crystals. Acta Metall. 29, 241–257.

Cuitiño, A.M., Ortiz, M., 1992. Computational modeling of single crystals. Modell. Sim. Mater. Sci. Eng. 1, 225–263.

Delaire, F., Raphanel, J.L., Rey, C., 2000. Plastic heterogeneities of a copper multicrystal deformed in uniaxial tension: experimental study and finite element simulations. Acta Mater. 48, 1075–1087.

Franciosi, P., Berveiller, M., Zaoui, A., 1980. Latent hardening in copper and aluminum single crystals. Acta Metall. 28, 273–283.

Franciosi, P., Zaoui, A., 1982. Multislip in f.c.c. crystals a theoretical approach compared with experimental data. Acta Metall. 30, 1627–1637.

Havner, K.S., 1992. Finite Plastic Deformation of Crystalline Solids. Cambridge University Press, Cambridge.

Hill, R., 1966. Generalized constitutive relations for incremental deformation of metal crystals. J. Mech. Phys. Solids. 14, 95–102.

Hill, R., Rice, J.R., 1972. Constitutive analysis of elastic–plastic crystals at arbitrary strain. J. Mech. Phys. Solids. 20, 401–413.

Kalidindi, S.R., Bronkhorst, C.A., Anand, L., 1992. Crystallographic texture evolution during bulk deformation processing of fcc metals. J. Mech. Phys. Solids. 40, 537–569.

Kocks, U.F., Tomé, C.N., Wenk, H.R., 2000. Texture and Anisotropy. Cambridge University Press, Cambridge.

Lee, E.H., 1969. Elastic–plastic deformation at finite strains. J. Appl. Mech. 36, 1–6.

Mandel, J., 1965. Généralisation de la théorie de la plasticité de W.T. Koiter. Int. J. Solids Struct. 1, 273–295.

Miehe, C., 1996. Multisurface thermoplasticity for single crystals at large strains in terms of Eulerian vector updates. Int. J. Solids Struct. 33, 3103–3130.

Needleman, A., Asaro, R.J., Lemonds, J., Peirce, D., 1985. Finite element analysis of crystalline solids. Comput. Meth. Appl. Mech. Eng. 52, 689–708.

Peirce, D., Asaro, R.J., Needleman, A., 1982. An analysis of nonuniform and localized deformation in ductile single crystals. Acta Metall. 30, 1087–1119.

Peirce, D., Shih, C.F., Needleman, A., 1984. A tangent modulus method for rate dependent solids. Comput. Struct. 18, 875–887.

Reid, C.N., 1973. Deformation Geometry for Materials Scientists. Pergamon Press, Oxford.

Rice, J.R., 1971. Inelastic constitutive relations for solids: an internal variables theory and its application to metal plasticity. J. Mech. Phys. Solids. 19, 433–455.

SARPP, 2002. Structural Analysis and Rock Physics Program. École Polytechnique, Palaiseau, France.

Schmid, E., Boas, W., 1935. Plasticity of Crystals. Chapman and Hall, London.

Shaw, J., Chang, B.-C., Iadicola, M., Leroy, Y.M., 2003. Thermodynamics of a 1-D shape memory alloy: modeling, experiments, and application. In: Proceedings of the SPIE 10th Annual International Symposium on Smart Structures and Materials, San Diego, CA.

Simo, J.C., Taylor, R.L., 1985. Consistent tangent operators for rate independent elasto-plasticity. Comput. Meth. Appl. Mech. Eng. 48, 101–118.

Taylor, G.I., 1938. Plastic strain in metals. J. Inst. Metals. 62, 307–324.

Taylor, G.I., Elam, C.F., 1923. The distortion of an aluminum crystal during a tensile test. Proc. Roy. Soc. London A. 102, 643–667.

Teodosiu, C., Sidoroff, F., 1976. A finite theory of elastoviscoplasticity of single crystals. Int. J. Eng. Sci. 14, 713–723.

Zarka, J., 1975. Modeling of changes of dislocation structures in monotonically deformed single phase crystals. In: Argon, A.S. (Ed.), Constitutive Equations in Plasticity. MIT Press, Cambridge, Mass, pp. 359–385.

Zikry, M.A., 1994. An accurate and stable algorithm for high strain-rate finite strain plasticity. Comput. Struct. 50, 337–350.